

GT2011-458' ,

TIME RESOLVED MEASUREMENTS IN THE DURHAM CASCADE

Felix Förster

Now at: Institut für Luftfahrtantriebe
University Stuttgart
Pfaffenwaldring 6
70569 Stuttgart
Deutschland

David Sims-Williams Grant Ingram* Robert Dominy

School of Engineering
and Computing Sciences
Durham University
Durham, DH1 3LE
United Kingdom
d.b.sims-williams@durham.ac.uk
g.l.ingram@durham.ac.uk
r.g.dominy@durham.ac.uk

ABSTRACT

This paper describes investigations into unsteady flow phenomena in a high turning linear cascade with a nominal steady flow. Traditionally time averaged instrumentation is used in such a cascade.

Detailed intermittency readings were taken inside the cascade using hot wires to highlight the detailed flow interactions of the passage vortex and the blade suction surface.

A new fast response five hole probe was built and tested against a hot-wire. Time-accurate measurements taken using this probe allowed an evaluation of the error made by using a probe with limited frequency response for the cascade measurements. This evaluation showed significant deviations in loss for regions of high unsteadiness, for instance the passage vortex.

The Reynolds stress tensor was measured at 101%, 115% and 128% axial chord and the deformation work was calculated for 126% axial chord. The deformation work shows regions of negative values and positive values. While negative values are associated with a production of turbulent k.e. from the mean kinetic energy, positive values may represent a gain of kinetic energy from the turbulence.

INTRODUCTION

This paper describes two sets of measurements in a well known low speed linear cascade. This so called “Durham Cascade” has provided a wealth of data on secondary flows [1], [2] and how they may be reduced by various techniques [3], [4]. These secondary flows arise from the turning of an inlet boundary layer and are a major source of loss inside high turning turbomachinery blade rows [5] the investigation of these flows has been the subject of much research [6], [7], [8] and recent work has examined the time-resolved nature of the flow even in low speed linear cascades [9].

The advances presented in this paper are twofold, firstly detailed measurements of intermittency on the suction surface are obtained using hot wire probe, these were at a considerably higher resolution than the results from [2] and used a new technique for evaluating intermittency that doesn't rely on empirical parameters to determine the intermittency threshold.

The second advance involves the design and assembly of a fast response pressure probe. The effects of using a probe with limited frequency response in a highly unsteady flow field are evaluated in this paper. This fast response probe also allows detailed measurements of all components of the unsteady flow in the cascade and the calculation of parameters such as the total deformation work.

* Address all correspondence to this author.

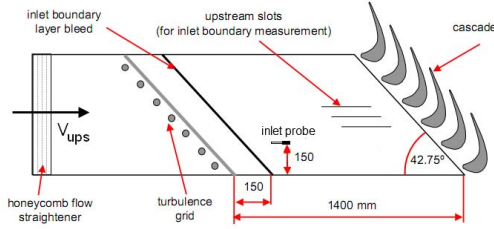


FIGURE 1. THE DURHAM CASCADE

Inlet Flow Angle	42.75°
Blade Exit Angle	-68.7°
Blade Axial Chord	181mm
Blade Pitch	191mm
Blade Span	375mm
Re	4.0×10^5
Dynamic Head	215 Pa
Inlet Velocity	19.1 ms^{-1}
Density of Air	1.179 kgm^{-3}
Dynamic Viscosity	$1.814 \times 10^{-5} Nsm^{-2}$

TABLE 1. DESIGN DATA AND STANDARD DAY

EXPERIMENTAL SETUP

The Durham cascade represents a rotor design with 110° of turning. A general arrangement of the cascade is shown in Fig. 1. The design data of the cascade is given in Table 1, the test rig is an 8x scale cascade and is therefore run at comparably low speeds to operate at the correct Reynolds number. Since the probe size and manufacturing tolerances are small compared to the dimensions of the blades, larger and hence cheaper instrumentation can be used than would be acceptable for a smaller facility.

Air is supplied to the test section by a variable-speed centrifugal fan. First the incoming air is filtered and then passes through various screens and settling chambers before emerging through a honeycomb into the working section. Next to that, there is a grid of bars mounted to give a turbulence intensity of around 5% and a length scale of around 9.4mm at the inlet. In order to achieve uniform inlet turbulence these bars are installed 1.4m in front of the blade's leading edge.

To establish appropriate boundary layer conditions, a bleed system is installed 150mm downstream of the turbulence grid. Both endwalls are provided with a bleed slot so that a symmetrical inlet flow is ensured. As the ambient conditions may change between the experiments, a reference condition was established

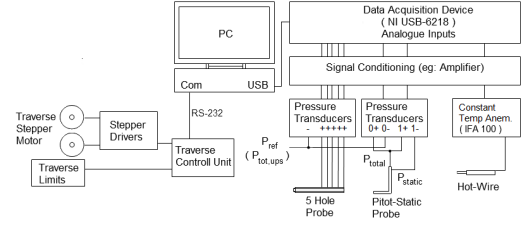


FIGURE 2. SCHEMATIC OF THE MEASUREMENT SETUP

known as the standard day. Table 1 lists the standard day conditions to which all pressure readings are normalised to by multiplication of the ratio of standard day dynamic pressure to actual dynamic pressure.

All measurement techniques provide the response of the respective probe as an analogue voltage signal. For the pressure probe work data was logged with National Instruments devices using burst mode conversion to achieve approximate simultaneous sampling (channel to channel data rate approximately two orders of magnitude above the frequency associated with unsteady flow features). A schematic overview of the test setup is provided in Fig. 2. The data are obtained by using the “Durham Software for Wind tunnels” an in-house suite of programs for data acquisition. The estimated uncertainties of the measured velocities and flow angles are $\pm 1m/s$ and $\pm 1^\circ$ respectively for conventional five hole probe and hot wire readings.

INTERMITTENCY

Intermittency is often used as a parameter to describe the degree of turbulence and its evolution for example inside a boundary layer. The parameter represents the time period for which the flow is turbulent relative to the entire sampling time. Low values of intermittency are therefore associated with laminar flow whereas high values indicate a region of high turbulence. Although large fluctuations of the signal (for example the voltage of a hot-wire) are characteristic for turbulent flow, the differentiation between laminar and turbulent portions is often more difficult under real conditions. Therefore a technique based on the TERA (Turbulent Energy Recognition Algorithm) method of Falco and Gendrich [10] was used to process the raw data. As pointed out by Moore [11], it is important to choose an algorithm that copes with the high free-stream velocity and pressure gradients in the cascade.

The function $\left| e \frac{\partial e}{\partial t} / \bar{E} \right|$ was calculated for the raw signal

where \bar{E} is the mean voltage and e is the fluctuation component. The approach in this work therefore differs slightly from the modifications to the TERA code presented by Moore [11] since the voltage is used instead of the effective velocity. As the main task is to determine the fluctuations with respect to a mean value it was found that the algorithm can be applied directly to

the raw voltage signal. A rolling average was carried out over 20 samples to smooth out short-term fluctuations and highlight the overall trend. A threshold is chosen above which the flow is taken to be turbulent. The intermittency is then calculated as the fraction of time for which the function is greater than the threshold. The main difference between these approaches and the TERA code is that the function is divided by the mean value to obtain a more constant threshold.

The threshold was defined by the difference of the root mean square and the arithmetic mean which provides a formal method to obtain the threshold. This method has the advantage that threshold is defined by a specific rule and no empirical parameters are needed, unlike both the TERA code and the method used by Moore. For the TERA code the rms value is multiplied by an empirical factor whereas Moore selected the threshold value by inspecting the rolling average graph.

To illustrate the effect of the whole procedure, an example is given in Fig. 3 where the rolling average is compared to the raw signal. For the rolling average the laminar and turbulent portions can be easily distinguished, whereas this is difficult for the corresponding section of the raw signal. As one can see the flow is mostly laminar and therefore represented by a low intermittency value of 0.2. The red line indicates the threshold in the rolling average plot.

FAST RESPONSE PROBE

Multi-hole pressure probes are widely used for steady state measurements, but rarely for unsteady flow experiments. For time-accurate measurements researchers generally prefer hot-wire systems due to their very high frequency response. But multi-element hot-wire probes are required to measure all three velocity components instantaneously, and these are very expensive and less robust than pneumatic probes. However, only multi-hole pressure probes allow the measurement of total pressures and velocities directly, which was outlined as a very important task for unsteady flow experiments by Bearman et al [12].

Even though pressure probes have some advantages, conventional multi-hole probes have a very limited frequency response. The frequency response of a conventional multi-hole probe with remote transducers is limited principally by distortion in the tubing between the probe head and the transducers. Specific frequencies are amplified as a result of resonance, and viscosity tends to damp high frequencies. Applying transfer function correction can allow correction of this tubing distortion up to frequencies of several hundred Hz (eg: Sims-Williams et al [13]). The achievable frequency response is ultimately limited by deteriorating signal to noise ratio at higher frequencies when only a small pressure signal reaches the transducer. The practical upper limit for this approach with remote transducer is about 1 kHz.

Extending probe response to higher frequencies is achieved here by building miniature pressure transducers into the rear of

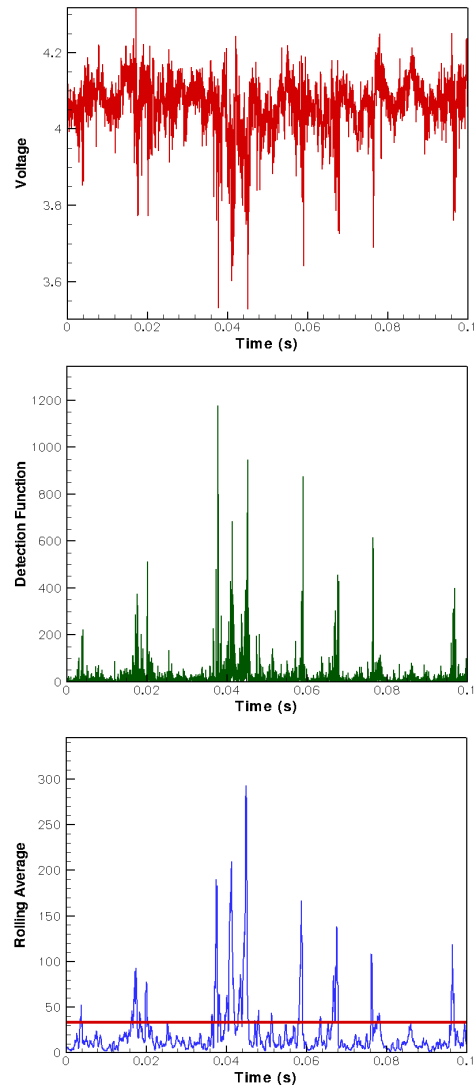


FIGURE 3. INTERMITTENCY DETECTION PROCEDURE

the probe head, essentially eliminating tubing distortion. The Kulite XCQ-80 pressure transducer [14] is small enough to store five in the probe head and still provide an adequate pressure sensitivity. The latter is essential for accurate measurements of the small differential pressures in the cascade. Rapid prototyping was used to manufacture the complex probe head including internal geometry with the required accuracy. Figure 4 provides details of the dimensions of the probe head, and Fig. 5 shows the size of one pressure transducer relative to a UK one pence coin and the probe head. Each transducer is connected to four signal wires (excitation and sense) and one plastic tube that delivers the reference pressure.

It should be noted that achieving a high frequency response

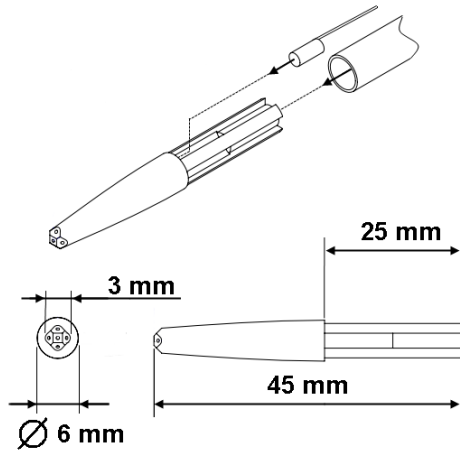


FIGURE 4. TECHNICAL DRAWING: PROBE HEAD

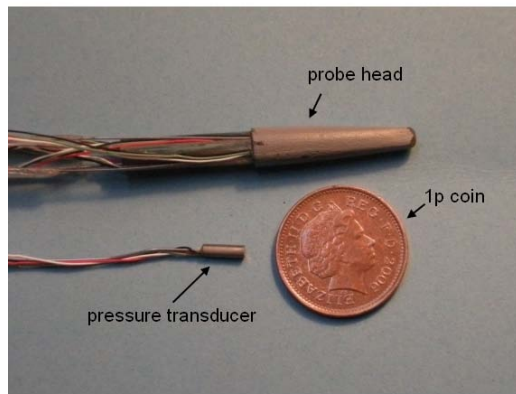


FIGURE 5. PROBE HEAD WITH PRESSURE TRANSDUCERS

is not achieved solely by employing fast response transducers and addressing tubing distortion. The frequency response also critically depends on the miniaturisation of the probe head in order to be able to resolve the small spatial scales associated with high frequency phenomena. This is a particular issue in low speed flows. The 3 mm probe head used here could be expected to allow adequate resolution of a 1000 Hz - 2000 Hz features at 30 m/s, corresponding to spatial scales of 15 mm - 30 mm. While the transducers themselves have a response exceeding 100 kHz it is the miniaturisation of the probe head which is the key attribute required to achieve a high frequency response in low speed flows.

VALIDATION

Although the Kulite transducers have a very high frequency response and the remaining tubes are fairly small, a validation was carried out. The 5H probe was set next to a hot-wire into

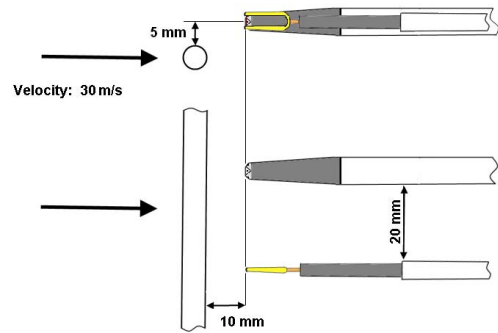


FIGURE 6. FREQUENCY RESPONSE VALIDATION

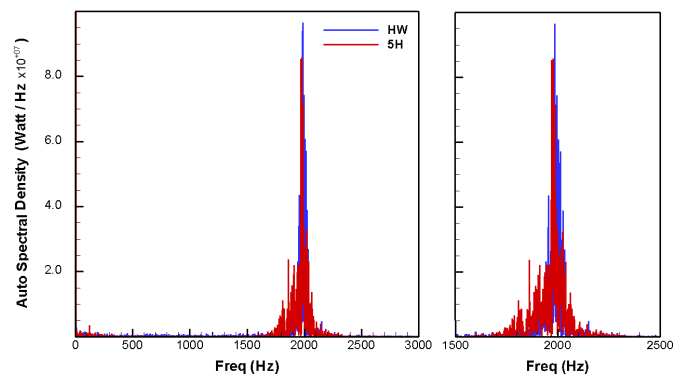


FIGURE 7. Auto Spectral Density

the wake of a cylinder. The resulting vortex shedding frequency was used to test the 5H probe directly against the hot-wire. To obtain frequencies of 1000 Hz and 2000 Hz, bars of 6 mm and 3 mm diameter respectively were used. The setup is shown in Fig. 6.

The results are found to be very sensitive to the position of the bar relative to the probe. Therefore the values given in Fig. 6 are meant to provide a general idea rather than an exact position. It must be ensured that the whole probe is affected by the passing vortex. An oscilloscope was used to check the voltage output and hence the position of the bar. When this shows a similar oscillation of transducer voltage in the centre hole and the one farthest away from the bar the vortex is detected by all holes and a measurement can be taken.

Applying the Fourier transform to the results the spectral density can be calculated as illustrated by Fig. 7. As one can see, the results of both probes are in good agreement since the graph shows nearly identical peaks.

With these results, the frequency response of the fast response pressure probe is proven up to frequencies of 2000 Hz. It

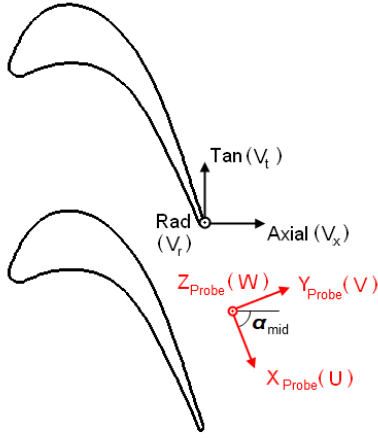


FIGURE 8. PROBE FIXED COORDINATE SYSTEM

was not possible to investigate the response for higher frequencies though the specification of the transducers suggest that the probe is capable to of resolving even higher frequencies. The difference between the effective velocity of the hot-wire and fast response probe was calculated and the standard deviation of the difference was found to be around 5 m/s, this suggests that a very pessimistic estimate of the uncertainty associated with fast response probes would be ± 2.5 m/s.

TURBULENT QUANTITIES

All turbulent quantities are given in the probe fixed coordinate system as specified in the Fig. 8. The velocity components are referred to as U, V and W.

The Reynolds stress tensor is an additional term in the Reynolds Averaged Navier Stokes (RANS) equations. It arises if the velocity in each direction is expressed in terms of a mean and fluctuating component: $U(t) = \bar{U} + u(t)$. The Navier Stokes equations can then be averaged to yield equations expressing momentum conservation for the averaged motion called the RANS equations. The average of the fluctuations is zero by definition, however this does not apply to their product. Considering an incompressible flow these additional terms are described by the Reynolds stress tensor (RST): $RST = \rho \overline{u_i u_j}$

For CFD simulation this additional term must be modelled by mathematical relationships between the Reynolds stresses and the mean velocities known as turbulence model. For the experiment, the instantaneous velocity components are given for each measurement point. A program was written to read the corresponding history file, calculate the mean and fluctuating components and determine the velocity correlations. As for the other presented quantities they are non-dimensionalised by the inlet velocity. As the density is assumed to be constant, the velocity

correlations are only scaled with velocity and density is ignored. For simplicity, these velocity correlations are still referred to as Reynolds stresses in this paper and the equation is given in Eqn. 1.

$$RST_{ND} = \frac{\overline{u_i u_j}}{V_{ups}^2} \quad (1)$$

Following Hinze [15] one can obtain the equation for kinetic energy of the mean motion from the equation of motion for an incompressible flow by multiplying it by the velocity vector. Applying the Reynolds's average procedure, this equation can be written as:

$$\begin{aligned} & \underbrace{\frac{1}{2} \frac{\partial}{\partial t} (\rho \bar{U}_i^2)}_I + \underbrace{\frac{\partial}{\partial x_j} \bar{U}_j \left(P + \frac{1}{2} \rho \bar{U}_i \bar{U}_j \right)}_{II} \\ & + \underbrace{\frac{\partial}{\partial x_j} \rho \overline{u_i u_j} \bar{U}_i - \frac{\partial}{\partial x_j} \mu \bar{U}_i \left(\frac{\partial \bar{U}_i}{\partial x_j} + \frac{\partial \bar{U}_j}{\partial x_i} \right)}_{III+IV} \\ & = \underbrace{\rho \overline{u_i u_j} \frac{\partial \bar{U}_i}{\partial x_j}}_V - \underbrace{\mu \left(\frac{\partial \bar{U}_i}{\partial x_j} + \frac{\partial \bar{U}_j}{\partial x_i} \right) \frac{\partial \bar{U}_i}{\partial x_j}}_{VI} \end{aligned} \quad (2)$$

The terms in the equation have the following physical interpretation [16]:

- I the rate of change of mean kinetic energy
- II the rate of convective transport of total pressure
- III the rate of mean kinetic energy transport by turbulent fluctuations
- IV the rate of mean kinetic energy transport by mean viscous stresses
- V the deformation work of the mean flow by turbulence stresses. The rate at which turbulence is produced from the mean flow as turbulent kinetic energy
- VI the rate of viscous dissipation through mean velocity gradients

This paper concentrates on the deformation work term since it is a key parameter for loss generation. It represents the rate of turbulence production from the mean flow and is defined in non-dimensional form by Maclsaac et al [9]:

$$\Psi_{i,j} = \frac{\overline{u_i u_j}}{U_{CL}^2} \cdot \frac{\partial \bar{U}_i / U_{CL}}{\partial x_j / C_x} \quad (3)$$

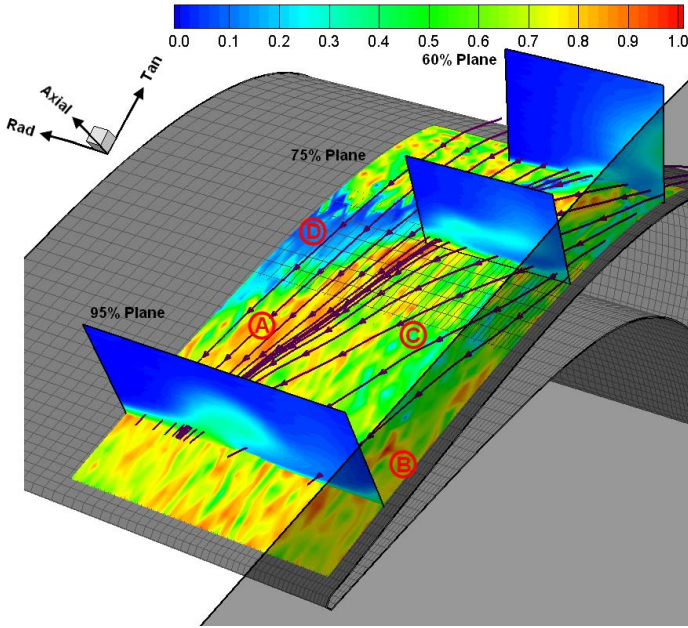


FIGURE 9. SUCTION SIDE: INTERMITTENCY

With summation over all nine terms the total deformation work is obtained which is plotted for the 126% plane. It is calculated by combining the measured Reynolds stresses with the velocity gradient calculated between the 124% and 128% plane.

INTERMITTENCY RESULTS

To determine the areas of laminar and turbulent flow, the suction side boundary layer was traversed with a normal hot-wire (Dantec 55-P01). A pin was attached to the probe stem that touched the surface of the blade. This ensured minimal aerodynamic vibrations and prevented damage to the probe.

The distance between the hot wire and the surface was set to 1mm. The area between 60% and 99% axial chord and up to 100mm from the endwall was traversed. The spatial resolution was set to 2mm in the axial and radial direction. The logging frequency was set to 50 kHz to ensure that all flow fluctuations were captured, a low-pass filter was used set to the value closest to the half of that frequency. At each grid point 16384 samples were taken.

Figure 9 shows the results with well-defined areas of laminar and turbulent flow, labelled A to D, on the suction side. To illustrate the adjacent flow field the C_{PO} distribution of some 60%, 75% and 95% planes traversed using a three hole probe are given along with the streamlines associated with the boundary layer.

Region A: Region A shows a trace of highly turbulent flow crossing the blade's surface. Its migration along the surface and the position at the trailing edge suggest that the high levels of turbulence are due to the suction side horseshoe vortex. This as-

sumption is confirmed since this trace nearly matches up with the aggregation of the boundary layer streamlines and the position of the loss cores shown in the planes.

Region B: A similar trace can be observed for the corner vortex. Located at the right side, the corner vortex becomes visible at about 75% axial chord and gains in size towards the trailing edge.

Region C: Region C is found between these two traces, downstream of the horseshoe vortex. It is known as a region of high free-stream velocity and therefore one would expect the flow to be developed fully turbulent. It is interesting to see that the region is mainly of moderate turbulence (about 0.5) and there are still observable locations where the intermittency is even lower (about 0.3). Higher values were not reached until the trailing edge. The form of the boundary layer is important for its contribution to aerodynamic losses. From a designer's perspective it is interesting to see that such an area of low intermittency can exist downstream of the trace of the horseshoe vortex. The question for designers will be how to extend this region and what the effect is in terms of loss reduction. It should also be noted that another trace of high intermittency is found right above the letter C (also highlighted in Fig. 10 A) and labelled PV). Although it is less distinctive than the traces discussed for region A and B, it is still observable. Since the trace is nearly parallel to the trace of the horseshoe vortex and the position coincides with the passage vortex seen in the planes, the trace is associated with this vortex. As the passage vortex keeps a certain distance to the surface, the trace is not as well-defined as the one of the horseshoe vortex, which stays close to the surface.

Region D: Upstream of the horseshoe vortex the situation is not as clear as before. One can see an area of very low intermittency next to the horseshoe vortex trace. Further upstream, a spotted area of moderate intermittency is found. This might possibly represent a transient boundary layer.

Measurements presented by Moore [2] suggest that the boundary layer is more laminar due to the strong acceleration over the first half of the blade. However, Moore used fixed slots to access the cascade and so hot-wire readings of a surface area comparable to this work had only been taken at four positions, namely 55%, 71%, 87% and 97% axial chord. Therefore the region of interest is not directly traversed, but averaged between the two slots.

A comparison is provided in Fig. 10 with the corresponding areas highlighted by blue lines. The position of the fixed slots is also included by the red lines. Note that the axial location is used for the 2D plots instead of aerofoil arc length.

Further evidence to support the idea that the flow is laminar in this region comes from Holley [7] who used an oil film interferometry measurement technique and inferred the skin friction coefficient of the suction side surface. For the discussed region the skin friction was constant. This suggests laminar flow in his cascade. Since Moore also found the boundary layer to be lam-

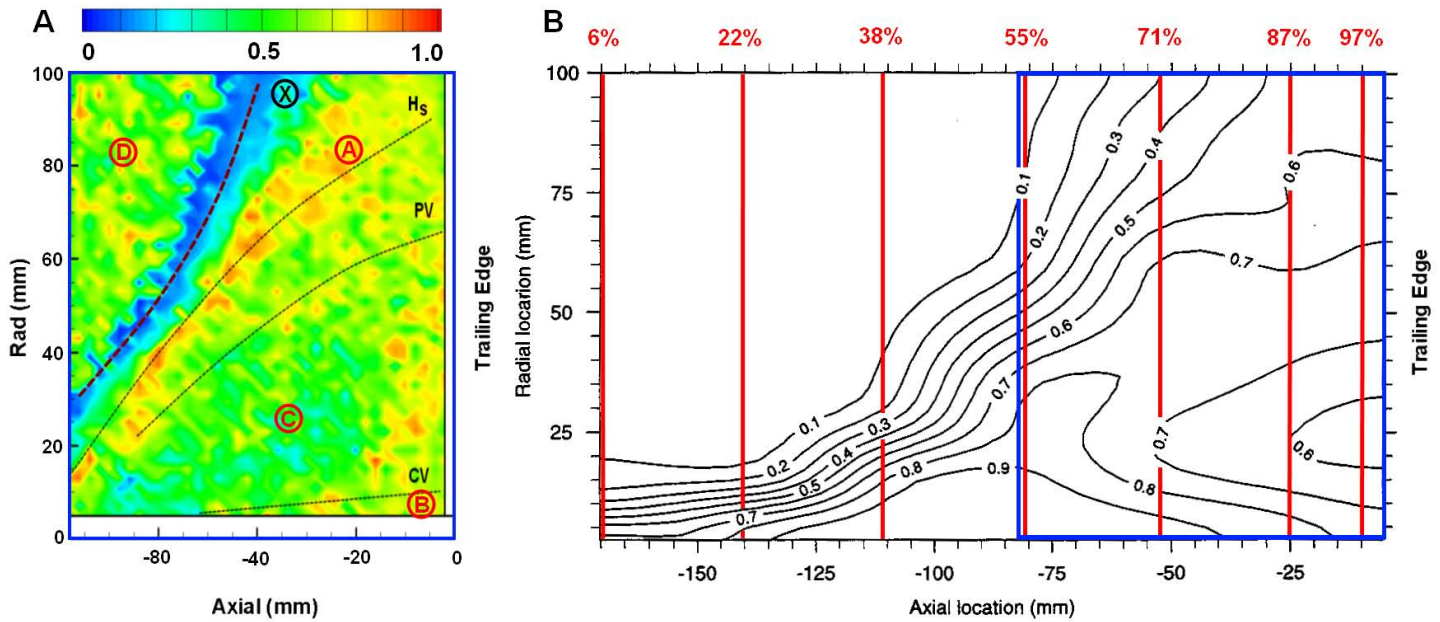


FIGURE 10. A) 2D Intermittency contour plot B) Comparison with the results of Moore [2]

inar at 55% axial chord, this assumption seems to be valid for measurements presented here.

As a result of this discussion, the spotted area is believed to reflect the free-stream turbulence rather than the situation inside the boundary layer. In order to calculate the displacement thickness, the 3H data was examined. However, the velocity profile was strongly affected by the interaction between the probe and the surface as the gap acts as a nozzle and causes the flow to accelerate. To obtain a more informative velocity profile a more detailed traverse using a hot-wire would be needed.

The region also features a trace of very low intermittency values in front of the horseshoe vortex as indicated by the line X in Fig. 10 A). A possible explanation is that although the measurements were carried out at constant distance to the surface, the boundary layer thickens in front of the horseshoe vortex. Therefore the hot-wire is able to pick up the laminar flow here whereas this is not possible further towards mid-span. The thickening might result from the blockage of the vortices and the diffusion of the incoming boundary layer fluid.

The spotted area is assumed to represent free stream turbulence rather than the boundary layer since these results are different from the situation found in similar cascades ([2], [7]).

TIME RESOLVED PRESSURE MEASUREMENTS

In this section the results of the newly built fast response pressure probe are presented. Since this was the first time this equipment had been used there was no experience about the occurring frequencies. For this reason, the 128% axial plane was

traversed with a rather high logging frequency of 10 kHz and the auto spectral density was calculated. The frequency stayed well below 1000 Hz. Since higher frequencies are supported by Kulite transducers according to the technical data sheet, the spectrum can be assumed to represent the frequencies in the cascade correctly. Nevertheless, the recording frequency was set to 5 kHz to provide a sufficient resolution of the flow quantities for all further measurement. The number of samples was set to 4096.

It is common practice in pressure measurements to use the voltage average of the probe signal as the input parameter for data processing. The probe signal is sampled and averaged. The calibration maps are applied to this mean value of the signal voltage and hence the subsequent calculations of the flow quantities are based on the voltage average as well. The resulting flow quantities are considered to represent the time averaged flow field as it is assumed that the real time average of a flow parameter is equal to the post processed value of the averaged voltage of the respective probe signal.

This approach is widely used as most conventional probes provide only a limited frequency response. Therefore it is not possible to measure all fluctuations correctly and calculate the time average from those, the idea of this approach is to smooth out all fluctuations by sampling over a sufficiently long time period in order to obtain a meaningful understanding of the time averaged flow.

In contrast to conventional probes, the new fast response pressure probe provides a high enough frequency response to resolve the unsteady fluctuations in the flow. The voltage signal

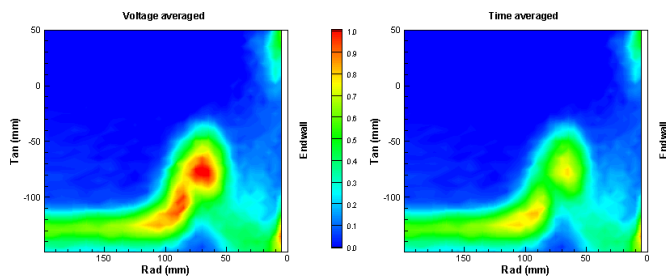


FIGURE 11. 128%: COMPARISON BETWEEN VOLTAGE AND TIME AVERAGED LOSS COEFFICIENT

of the probe is stored as a function of time in the history file. All calibration maps are applied to the time resolved voltage signal and the resulting flow quantities are added to the history file. Finally, the time average is calculated directly from the time resolved flow quantities. Assuming that the instantaneous flow is measured correctly, this approach provides the correct time averaged flow field.

As the instantaneous flow field can now be measured by the means of a pneumatic probe, both procedures can be applied to the same raw data to evaluate the approach used so far. For this purpose mean quantities are compared. In the following results obtained by the method described first are labelled “Voltage Averaged” whereas “Time Averaged” refers to averaging the quantity after applying the calibration.

Figure 11 shows the C_{PO} distribution of the 128% plane. In theory, the value should not depend on the point at which the time mean value is calculated during processing. However, a substantial discrepancy for the loss cores is found in Fig. 11.

Since the results are based on the same raw data, the subsequent processing must cause the differences in loss. Therefore one can also assume that this is caused by a systematic error. An explanation can be found by considering a simpler case:

Imagine a 5H probe which is exposed to a flow with varying yaw angle. The difference in pressure between two holes is used to determine the flow direction. Knowing the pitch and yaw angles, the total and dynamic pressure can be obtained by means of the probe’s calibration map. These parameters can be used to derive further flow quantities.

Figure 12 shows the time trace of the flow direction and the resulting probe signal along with a idealised calibration map of a 5H probe. The inclination of the flow the probe is exposed to is plotted in Fig. 12a along with the voltage signal of the holes sensitive to a change in yaw angle (Fig. 12b). As this is a fictitious example, the pitch angle can be set to 20° to highlight the discussed feature. The calibration map (Fig. 12c) illustrates the relationship between C_{Ptot} and the yaw angle for constant pitch angles. For convenience, only three pitch angles are shown.

The difference between the two averaging methods can now

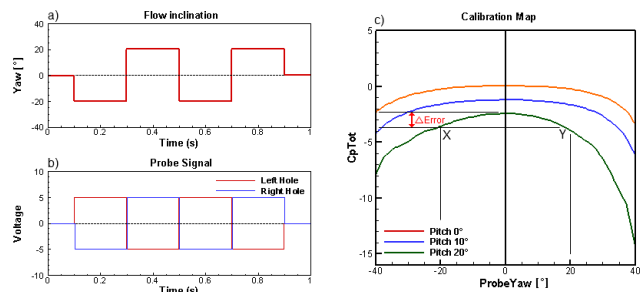


FIGURE 12. SIMPLIFIED EXAMPLE OF THE DATA PROCESSING

be explained. For the “Voltage Averaged” both signals are sampled and averaged. As the signals are in perfect anti-phase, the difference of the averaged signals is zero and therefore the mean yaw angle is zero as well (dotted lines in Figs. 12a-b). In the next step the calibration map is used to obtain the corresponding C_{Ptot} . For this example, C_{Ptot} is found to be -2 for a mean yaw angle of 0° and a pitch angle of 20° .

For the “Time Averaged” the yaw angle is time resolved and exhibits the same shape as the real flow in Fig. 12a. Thus the calibration map is read for instantaneous values as well, namely -20° and 20° . The corresponding C_{Ptot} values are found at the positions labelled X and Y in the calibration map. For this approach the yaw angle is a function of time and so is the C_{Ptot} (even if the function is constant in this example because the corresponding value is -4 for $\pm 20^\circ$). The last step is to average that function which leads to a time averaged C_{Ptot} of -4 and hence differs substantially from the value found for the previous method.

Even if the example is highly simplified, it is very useful to illustrate the discrepancy between voltage and time averaged results as a consequence of the nonlinear relationship between C_{Ptot} and the yaw angle. Therefore the time averaged C_{Ptot} is not equal to the C_{Ptot} found for the time averaged yaw angle, but differs substantially. It also shows that the resulting error increases for large fluctuations. A variation of $\pm 5^\circ$ for the flow inclination for instance would cause a smaller error.

For the actual experiments, every nonlinear operation will result in an additional error. What was described for the yaw angle also applies to the relationship between C_{Ptot} and the pitch angle. As a similar calibration map is used to calculate the dynamic pressure, the derived velocities and all subsequent calculations suffer even more from the error propagation.

Although the pitch and yaw angles are also affected the relationships between the flow angle and the pressure difference of the respective holes are nearly linear. Pressure transducers generally also have a linear calibration characteristic. Therefore the deviations of time and voltage averaged values are relatively small for the pitch and yaw angle.

As loss and its production are key parameter in turbomachin-

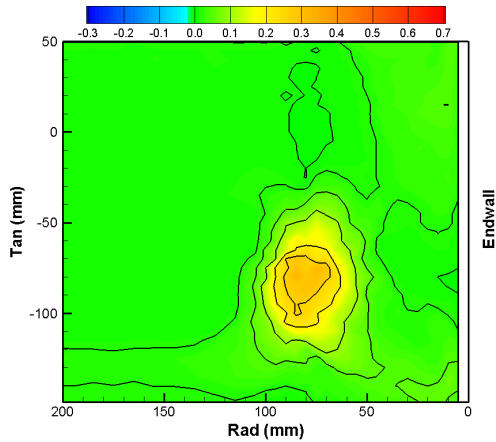


FIGURE 13. 128%: TOTAL PRESSURE ERROR COEFFICIENT

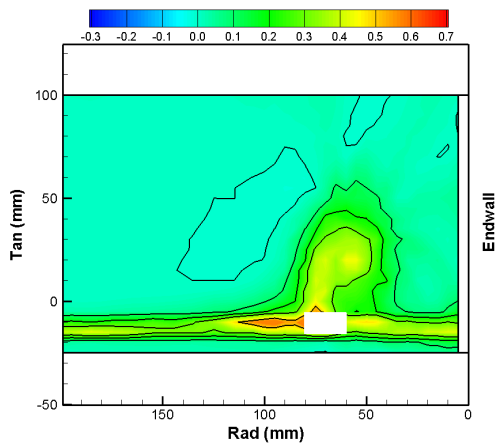


FIGURE 14. 101%: TOTAL PRESSURE ERROR COEFFICIENT

ery research, an error coefficient is presented in Fig. 13. Here, the difference in total pressure is non-dimensionalised by the dynamic head of the inlet. In order to take fluctuations at the inlet into account, the total pressure was also normalised for standard day conditions.

As one can see in Fig. 13, high deviations are mainly found for the regions associated with the vortical structures. Here the flow is inherently unsteady and so the instantaneous values differ notably from the mean value.

As mentioned before, the investigation was carried out for the 128% plane. The vortices mix out with the freestream downwards the blade. This progress is already widely advanced at this position and so large fluctuations could already be attenuated due to mixing. Therefore one would expect higher deviations closer to the trailing edge. This is confirmed by traversing the 101% plane. Figure 14 shows the non-dimensionalised error in total pressure.

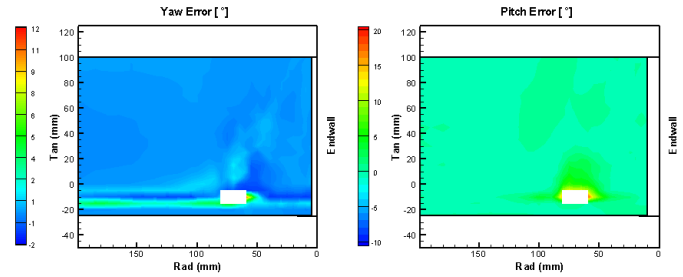


FIGURE 15. 101%: DEVIATIONS IN YAW AND PITCH ANGLE

As for the 128% plane, the loss cores of the suction side horseshoe vortex and the passage vortex are most affected by the averaging method. However, compared to the 128% plane the error caused has almost doubled. The figure also contains a blanked area, where the calibrated range of the probe was exceeded. Although the calibration was performed to capture the full range of expected yaw and pitch, instantaneous flow angles were found to exceed the calibration range even though the averaged flow was within it.

In addition to the vortex centres, high deviations are also found for the blade wake. This suggests that the shedding vortex at the trailing edge causes an unsteady flow. However, a significant error is only seen at 101% (Fig. 14) and not at 128% (Fig. 13). Therefore this vortex seems to produce less unsteadiness compared to the secondary flow vortices as the mixing out is already complete in the 128% plane.

Figure 15 shows the yaw and pitch error at 101%, where there are substantially higher deviations than for the 128% plane. So at 101% the instantaneous flow features exhibit large enough fluctuations that even the small non-linearity of the pressure-flow angle-relationship causes significant errors. Since the discrepancy associated with the blade wake is only seen for the yaw angle, the shedding vortex is confirmed as the source of the unsteadiness. Since it is basically a 2D feature, it is likely to affect the yaw angle but not the pitch angle.

A comparison of pitch averaged quantities is included for the 128% plane. In Fig. 16 the pitch averaged loss is plotted against the radial position for time and voltage averaged methods. As before the same raw data was used and the only difference is the point when the mean value is calculated. The loss obtained from a conventional 5H probe is given as well. The data in Fig. 16 was adjusted to give the same mid-span loss. For the voltage and time averaged readings the relative adjustment required for this is small at less than 0.01 but for the conventional five hole probe the size of the adjustment is somewhat larger at 0.05. This suggests that the fast response probe may be understating the level of losses somewhat.

All graphs coincide very well for mid-span and near the endwall, but show substantially different peaks for the vortices. As

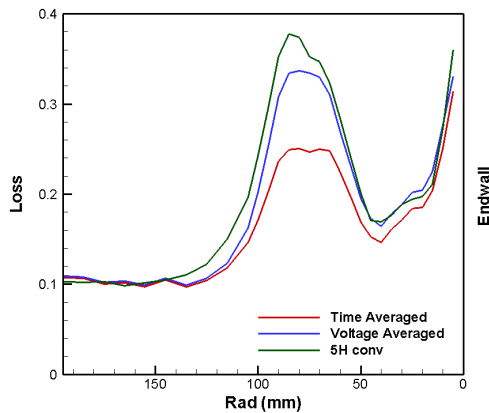


FIGURE 16. 128%: COMPARISON OF PITCH AVERAGED LOSS

the “Voltage Averaged” approach is the one used for all conventional probes, their graphs ought to be similar. The voltage averaged graph follows the conventional probe closely but peaks at a slightly lower value. The conventional probe data actually comes from a different passage in the cascade due to new probe stem arrangements for the fast response probe. If the position of the probe differs slightly, then the loss peak of the vortex might not be caught by the probe. The key point however is that the differences between the processing the same data in two ways (voltage and time averaging data) is much larger than the difference from using two different probes. Hence the difference from the time averaged graph is attributed to the assumed linearity of the calibration map. The actual nonlinear relationships cause significant deviations for sufficiently unsteady flow.

TURBULENCE QUANTITIES

As the fast response probe provides instantaneous information about the flow field, turbulent quantities such as the Reynolds stress tensor and turbulent kinetic energy can be calculated. These quantities are plotted as non-dimensional values defined earlier. Measurements were carried out for the 101%, 115% and 128% plane to examine the evolution downstream the blade. It should be noted that the Reynolds stresses are given for the probe fixed coordinate system as defined earlier.

Figure 17 shows the six Reynolds stresses for the 101% plane. For this plane the highest values were measured, especially for the \overline{uu} which is the dominant parameter in this plane. For the cross correlations the maximum is found for \overline{uw} and is believed to be the result of the strong interaction of the passage and shed vortex.

The blade wake is of the same magnitude as the passage vortex for \overline{uu} and \overline{vv} , but displays noticeable lower values in the \overline{ww} distribution. Consequently, the blade wake can only be identified

for the \overline{uv} correlations and not for the remaining shear stresses. This supports the idea that the shedding vortex behind the blade is a 2D phenomenon.

The 128% plane was mainly measured to check the technique and the processing software it had been previously traversed by Moore [11]. The results are in good agreement, and therefore are not shown. The present results tend to be higher, especially for the turbulent k.e.. However, the setup of the cascade was changed since Moore’s measurement including the blade span and the inlet boundary layer profile (see [17] for further details) which is very likely to affect the turbulence quantities. Furthermore, Moore has used a single-wire technique which requires several readings. As the fast response probe measures all velocity components almost simultaneously, this potential error source is eliminated. Overall though the fast response pressure probe is therefore a valid alternative to the hot-wire technique for measuring the Reynolds stress tensor.

DEFORMATION WORK

Besides contributing to our understanding of the secondary flow field, the investigation was also motivated by the results presented by Maclsaac et al [9], who calculated the deformation work. For simplicity, the total deformation work is simply referred to as deformation work from here onwards. This term arises from the equation of mean kinetic energy as detailed earlier and can be thought of as the working of the Reynolds stress against the mean velocity gradient of the flow, exactly as the viscous stresses resist deformation by the instantaneous velocity gradients [18]. In this context negative values represent a loss of mean kinetic energy to the production of turbulent k.e. and thus to the generation of total pressure loss. The physical implication is that the energy is transferred through a stretching process of turbulence vortices due to the mean motion. Finally, the transfer from the turbulent k.e. to loss is caused by viscous dissipation which points out the importance of Reynolds stresses to the generation of total pressure loss.

However, certain turbulent flows also show positive deformation work as it is the case for several measurements in linear cascades ([19], [20], [9], [8]). The conclusion, that this implies a transfer of energy back to mean kinetic energy and therefore a gain from turbulence is not necessarily true as one must also consider the terms that are associated with dissipation (especially in the equation of mean turbulent kinetic energy as detailed by Hinze [15]). Nevertheless, this is still possible as reported by Moore et al. [16] for the deformation work in the stream-wise direction.

Although derived for the mean flow field, the deformation work is affected by the instantaneous velocity gradients and would therefore be influenced by a periodic movement of the entire vortex structure.

To ensure that the same situation is found for the Durham

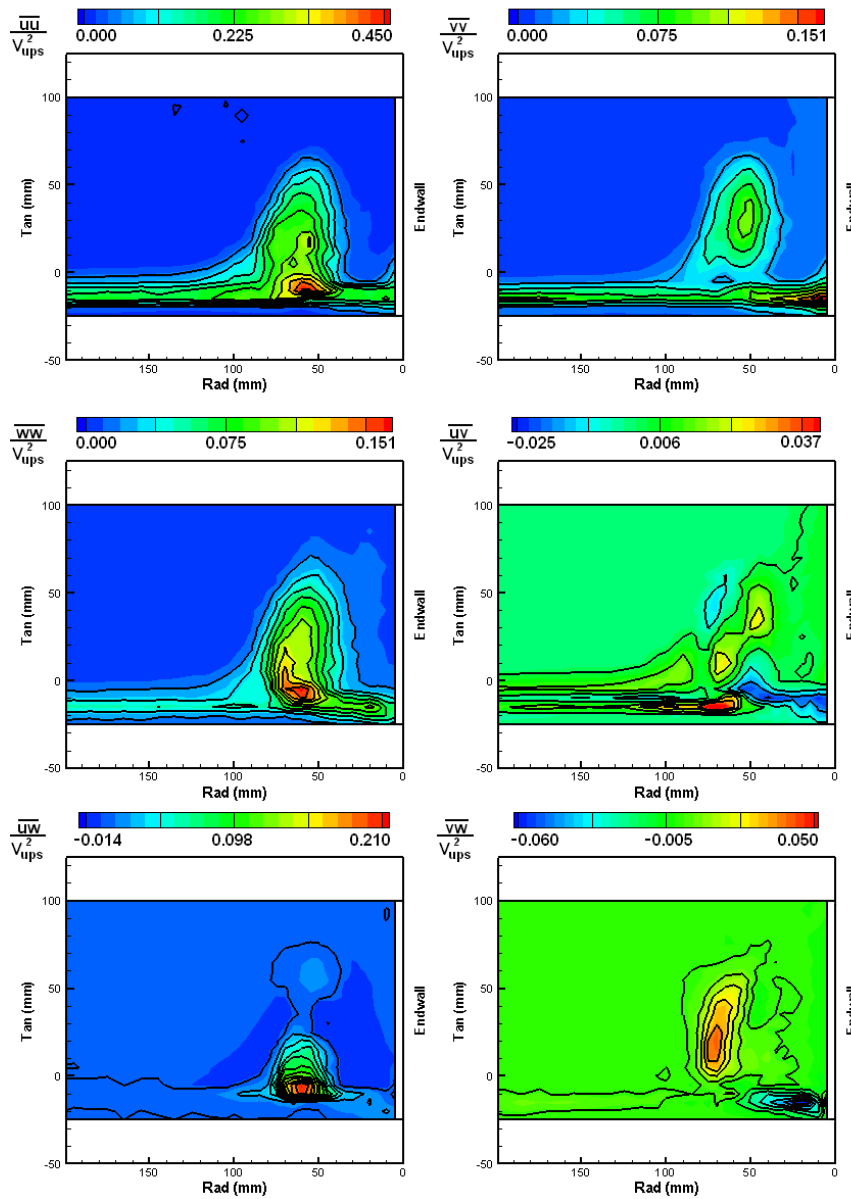


FIGURE 17. 101%: Non-dimensionalised Reynolds stresses

Cascade, the deformation work was calculated. For this purpose a second plane was traversed in addition to the 128% plane. The data were interpolated between the two planes by the Tecplot Krige algorithm and the velocity gradients were calculated. In order to reduce interpolation errors, the 124% plane was chosen as this results in the same spacing for all three directions. The deformation work was then calculated between these planes at the 126% plane and is presented in Fig. 18. It also includes the secondary velocity vectors and lines of constant total pressure to highlight the vortex structures and the blade wake.

As one can see, well-defined regions of positive and negative deformation work are found. The highest positive values are found for the centre of the passage vortex. The region between passage and horseshoe vortex on the other hand is dominated by negative values. For the blade wake, the upper half is positive whereas the lower half remains negative. A similar observation can be made for the horseshoe and corner vortex.

The results are in good agreement with the results presented by Maclsaac et al [9]. The regions of positive and negative values coincide very well, except for the blade wake. Here he found a

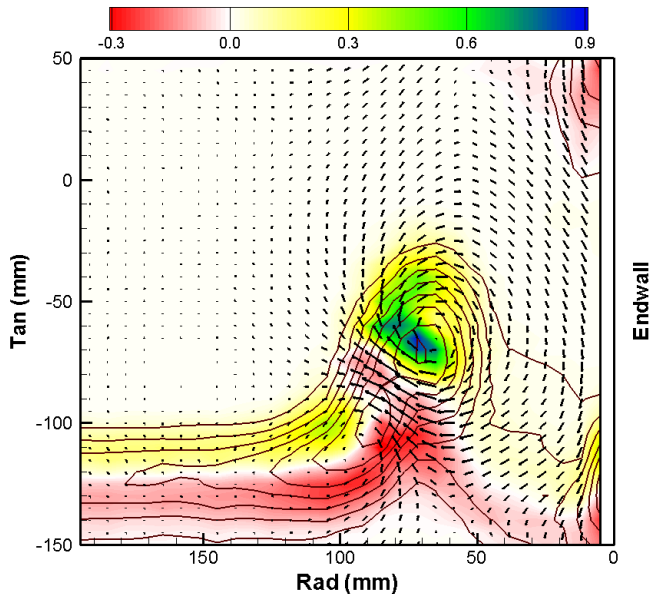


FIGURE 18. 126%: Total Deformation Work

small band of positive values for the blade wake surrounded by negative values rather than a partition in an upper and lower half. Also the peak value of the passage vortex was found to be higher in this work.

Although the deformation work was calculated by the same equation, it should be noted that Maclsaac could not use experimental data to calculate the axial mean velocity gradient as the axial distance between the traversed planes was too big. Therefore the expressions had to be derived by a method similar to that reported by Gregory-Smith et al [1]. A comparison between the approaches in order to investigate their effect on the resulting deformation work was not undertaken in this work, but assumed to be small. The decisive factor for the approach used here was the ability of the fast response probe to measure Reynolds stresses in one run. Otherwise the effort involved in measuring a second plane might not be justified.

CONCLUSIONS

1. Detailed intermittency readings have been conducted on the suction side of the Durham Cascade using a robust intermittency detection algorithm that does not require empirical judgements.
2. These investigations reveal a noticeable recovery of the intermittency level behind the suction side limb. Although expected to be fully turbulent, the results suggest that a new boundary layer starts laminar but becomes turbulent towards the trailing edge. There may be opportunities to exploit this in the design of new blades.

3. A new fast response five hole probe was built and tested against a hot-wire and demonstrated a frequency response of at least 2000 Hz with the potential for a much faster response.
4. Time-accurate measurements allowed an evaluation of the error made by using a probe with limited frequency response for the cascade measurements. This evaluation showed significant deviations in loss for regions of high unsteadiness, for instance the passage vortex.
5. Bigger deviations were found at axial chords closer to the trailing edge as they feature a higher level of unsteadiness.
6. The primary cause of these deviations was found to be caused by the non-linearity of the probe's calibration map. The biggest influence is on total pressure but pitch and yaw angle errors are introduced where there are very high levels of unsteadiness.
7. Where required, the frequency response of pressure probes should be evaluated to ensure that it is sufficient. This is less important if it is intended to compare measurements of different geometries, for instance different blade designs for a cascade. In this case, one could assume that all measurements are affected equally.
8. The Reynolds stress tensor was measured at 101%, 115% and 128% axial chord. Generally, the individual distributions are consistent with the structures of the mean flow field. High values were found for the regions associated with the passage vortex and the blade wake.
9. The deformation work has been calculated for the 126% axial plane and shows regions of negative values and positive values.

REFERENCES

- [1] Gregory-Smith, D. G., Graves, C., and Walsh, J. A., 1988. "Growth of secondary losses and vorticity in an axial turbine cascade". *ASME J. Turbomach*, **110**, pp. 1–8.
- [2] Moore, H., and Gregory-Smith, D. G., 1996. "Transition effects on secondary flows in a turbine cascade". *ASME 96-GT-100*.
- [3] Ingram, G. L., Gregory-Smith, D., and Harvey, N., 2005. "The benefits of turbine endwall profiling in a cascade". *Proc. IMechE*, **219**, p. A.
- [4] Bagshaw, D. A., Ingram, G. L., Gregory-Smith, D., and Stokes, M. R., 2008. "An experimental study of three-dimensional turbine blades combined with profiled endwalls". *Proc. IMechE*, **222**, p. A.
- [5] Sieverding, C. H., 1985. "Recent progress in the understanding of basic aspects of secondary flows in turbine blade passages". *Transactions of the ASME, Journal of Engineering for Gas Turbines and Power*, **107**, pp. 248–257.
- [6] Sieverding, C. H., and Bosche, V. D., 1983. "The use of coloured smoke to visualize secondary flows in a turbine-

- blade cascade”. *Journal of Fluid Mechanics, Cambridge University Press*, **134**, pp. 85–89.
- [7] Holley, B. H., and Langston, L. S., 2009. “Surface shear stress and pressure measurements in a turbine cascade”. *ASME J. Turbomach*, **131**.
- [8] Perdichizzi, A., Marina, U., and Zunino, P., 1992. “Reynolds stress distribution downstream of a turbine cascade”. *Experimental Thermal and Fluid Science*, **5**, pp. 338–350.
- [9] MacIsaac, G. D., Sjolander, S. A., and Praisner, T. J., 2010. “Measurements of losses and reynolds stresses in the secondary flow downstream of a low-speed linear turbine cascade”. *ASME GT2010-22727*.
- [10] Falco, R. E., and Gendrich, C. P., 1988. “The turbulent burst detection algorithm of z. zaric”. In Zoltan Zaric memorial conference.
- [11] Moore, H., 1995. “Experiments in a turbine cascade for the validation of turbulence and transition models”. PhD thesis, School of Engineering and Computer Sciences, University Durham.
- [12] Bearman, P. W. and Harvey, J. K. and Stewart, J. N., 1997. “Two and three component velocity measurements in a wind tunnel using piv”. *Wind Tunnels and Wind Tunnel Test Techniques, Cambridge UK*.
- [13] Sims-Williams, D. B., and Dominy, R. G., 1998. “The validation and application of a 5-hole pressure probe with tubing transfer function correction for time-accurate measurements in unsteady flows”. *Second MIRA International Conference on Vehicle Aerodynamics*.
- [14] Kulite Semiconductor Products Inc. Technical data: Kulite xcl-80. available at http://www.kulite.com/pdfs/pdf_Data_Sheets/XCQ-080.pdf.
- [15] Hinze, J. O., 1975. *Turbulence*, 2 ed. McGraw-Hill Companies.
- [16] Moore, J., Shaffer, D. M., and Moore, J. G., 1987. “Reynolds stresses and dissipation mechanisms downstream of a turbine cascade”. *ASME J. Turbomach*, **109**, pp. 258–267.
- [17] Bagshaw, D., Ingram, G., Gregory-Smith, D., and Stokes, M., 2006. “A turbine cascade facility for secondary flow research”. *ASME Paper GT2006-90868*.
- [18] George, W. K., n.d.. *Lectures in Turbulence in the 21st Century*. Department of Applied Mechanics.
- [19] Gregory-Smith, D. G., Walsh, J. A., and Graves, C., 1988. “Turbulence measurements and secondary flows in a turbine rotor cascade”. *ASME J. Turbomach*, **110**, pp. 479–485.
- [20] Gustafson, R., Mahmood, G., and Acharya, S., 2007. “Aerodynamic measurements in a linear turbine blade passage with three-dimensional endwall contouring”. *ASME GT2007-28073*.

NOMENCLATURE

C_{PO}	Pressure loss coefficient
$C_{P_{tot}}$	Probe total pressure coefficient
\bar{E}	Mean voltage
e	Fluctuating voltage
RST	Reynolds stress tensor
Re	Reynolds number based on exit velocity and axial chord
U, V, W	Steady velocity components relative to probe
u, v, w	Fluctuating velocity components relative to probe
V_{ups}	Inlet velocity to the cascade
$\Psi_{i,j}$	deformation work term
ρ	density